ReciPro: free and open-source multipurpose crystallographic software integrating a crystal model database and viewer, diffraction and microscopy simulators, and diffraction data···

Seto, Yusuke

Ohtsuka, Masahiro

ReciPro: free and open-source multipurpose crystallographic software integrating a crystal model database and viewer, diffraction and microscopy simulators, and diffraction data analysis tools

Yusuke Seto and Masahiro Ohtsuka

IUCr Journals
CRYSTALLOGRAPHY JOURNALS ONLINE

ReciPro: free and open-source multipurpose crystallographic software integrating a crystal model database and viewer, diffraction and microscopy simulators, and diffraction data analysis tools

Yusuke Seto[a]* and Masahiro Ohtsuka[b]

[a]Department of Planetology, Graduate School of Science, Kobe University, 1-1 Rokkodai-cho Nada-ku, Kobe 657-8501, Japan, and [b]Advanced Measurement Technology Center, Institute of Materials and Systems for Sustainability, Nagoya University, Furo-cho Chikusa-ku, Nagoya 464-8603, Japan. *Correspondence e-mail: seto@crystal.kobe-u.ac.jp

ReciPro is a comprehensive multipurpose crystallographic program equipped with an intuitive graphical user interface (GUI), and it is completely free and open source. This software has a built-in crystal database consisting of over 20 000 crystal models, and the visualization system can seamlessly display a specified crystal model as an attractive three-dimensional graphic. The comprehensive features are not confined to these crystal model databases and viewers. It can smoothly and quantitatively simulate not only single-crystal and/ or polycrystalline (powder) diffraction patterns of X-ray, electron and neutron diffraction of a selected crystal model, based on the kinematic scattering theory, but also various electron diffraction patterns and high-resolution transmission electron microscopy (TEM) images, based on the dynamical scattering theory. The features of stereographic projection of crystal planes/axes to explore crystal orientation relationships and the semi-automatic diffraction spot indexing function for experimental diffraction patterns assist diffraction experiments and analyses. These features are linked through a user-friendly GUI, and the results can be synchronously displayed almost in real time. *ReciPro* will assist a wide range of crystallographers (including beginners) using X-ray, electron and neutron diffraction crystallography and TEM.

1. Introduction

X-ray, electron and neutron diffraction crystallography have long been powerful tools in numerous fields including physical, chemical, biological and planetary sciences. X-ray and neutron diffraction methods are widely employed because of the easy availability of flexible laboratory X-ray sources, high-flux synchrotron radiation facilities and modern neutron sources, and established crystal structure analysis methods such as Rietveld fitting (Rietveld, 1969). Electron diffraction methods employing a finely focused electron probe *via* transmission electron microscopy (TEM) and/or scanning TEM (STEM) are also popular in local analysis at the sub-ångström to (sub-)nanometre scale, and atomic column-by-column imaging to reveal the crystal structure directly is also becoming a common practice with the advances in and spread of lens aberration correction technologies. The crystal-lographic information provided by these techniques is often the first step in basic and applied research on crystalline materials. A challenge of TEM is that novice crystallographers often have difficulty understanding the symmetry of a crystal structure from its diffraction pattern and the relationship
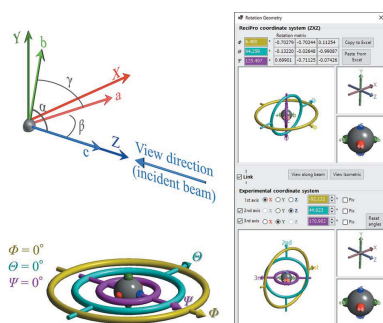
between real space and reciprocal space. Electron diffraction patterns are not intuitive because of the dynamical scattering effect, namely multiple electron scattering, and atomic resolution S/TEM images are further modulated by the aberration of electromagnetic lenses. Thus, a detailed comparison between their precise simulations and experimental data is indispensable to achieve a quantitative analysis.

The solution to such problems faced by numerous non-expert crystallographers is the use of crystallographic software that integrates features such as visualization and manipulation of crystal structure models, simulation of diffraction patterns and S/TEM images, and diffraction data analysis tools with an intuitive graphical user interface (GUI) and that can be easily installed without the cost of setting up a running environment. Software development in the field of crystallography is now advanced, with not only commercial software available but also free and open-source software. *VESTA* (Momma & Izumi, 2011), *VMD* (Humphrey *et al.*, 1996), *XcrysDen* (Kokalj, 1999) and *CrystalMaker* (http://crystalmaker.com) are very popular and widely employed programs for the visualization and modelling of crystal structures, and single-crystal and/or polycrystalline (powder) diffraction simulators using the kinematic scattering approximation for X-rays, electrons and neutrons are also implemented in some of them. *Tempas* (Kilaas *et al.*, 1987), *JEMS* (Stadelmann, 1987), *xHREM* (Ishizuka & Uyeda, 1977), *QSTEM* (Koch, 2002), *MULTEM* (Lobato & Van Dyck, 2015), *Prismatic* (Pryor *et al.*, 2017) and *Dr. Probe* (Barthel, 2018) are currently maintained GUI-based S/TEM simulation programs based on the dynamical electron scattering theory. A recent trend has been the development of Python-based software which can be flexibly customized by even non-expert programmers, such as *ASE* (Larsen *et al.*, 2017) and *pymatgen* (Ong *et al.*, 2013) for handling atoms and crystal models, *diffPy* (Juhás *et al.*, 2015) for powder diffraction data analyses, and *abTEM* (Madsen & Susi, 2021) and *py_multislice* (Brown *et al.*, 2020) for S/TEM image simulations. Most of these programs were developed for specific purposes (*e.g.* crystal structure visualization, diffraction or image simulation) and offer a number of excellent features. By using these programs in a complementary manner, a variety of crystallographic analyses can be performed. Although this is a good situation for researchers with sufficient PC skills and crystallographic expertise, those who do not have such skills may have difficulty in preparing the execution environment (such as Python and an external package) and setting up the desired crystal structures and experimental conditions for the software, and in some cases may even give up using the software. Therefore, a self-contained and standalone program that integrates various crystallographic functions, equipped with user-friendly GUIs, is still essential to encourage non-expert researchers.

Here, we have developed a completely free and open-source program, *ReciPro*, designed to satisfy such demands. *ReciPro* provides a sophisticated and seamless integration of a complete package of crystallographic functions, from visualization of crystal structures to quantitative simulation of diffraction patterns and TEM images. *ReciPro* can be easily installed and run on Microsoft Windows operating systems by simply pre-installing the Microsoft .NET Desktop Runtime 6.0.

2. Software design

ReciPro is a self-contained standalone program written in C++, C# and OpenGL Shading Language (GLSL). Its user-friendly GUI allows users to manipulate crystallographic information such as space groups, lattice parameters and atomic positions, visualize a crystal structure in 3D graphics, display a stereonet to represent the stereographic projection of crystal planes/axes, assist spot indexing in experimental diffraction patterns, calculate quantitative electron, X-ray and neutron diffraction patterns, and simulate high-resolution TEM (HRTEM) images, without association with other software packages that require labour to remake input files suited
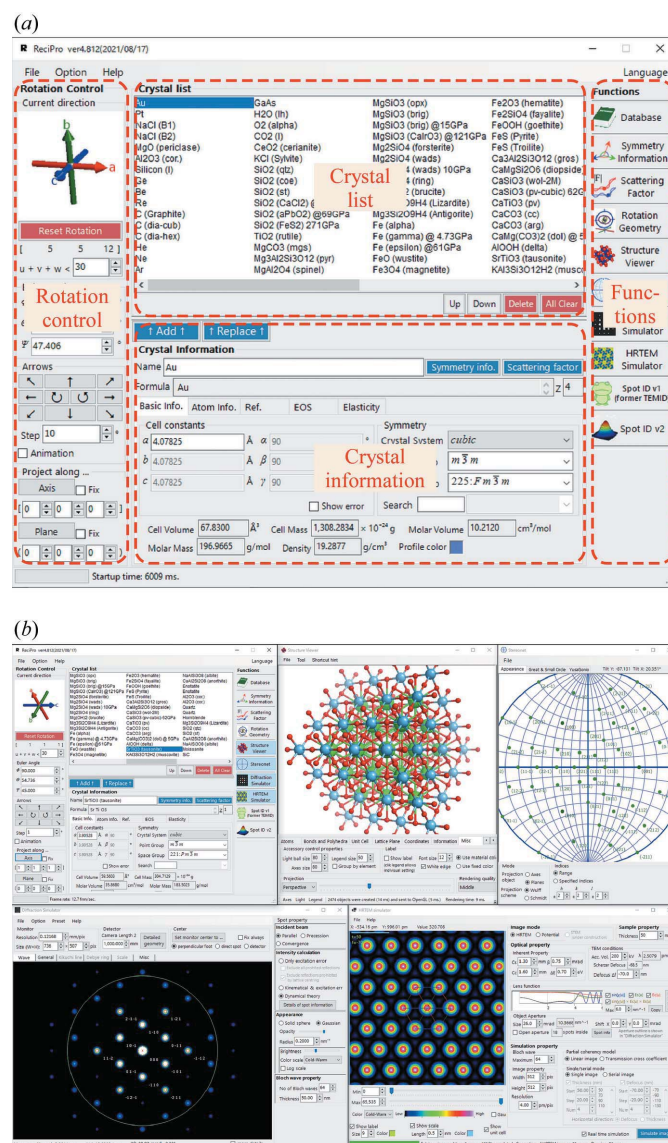

Figure 1
(*a*) The main window of *ReciPro*. (*b*) A snapshot with multiple functions open at the same time. To see the real-time calculation while rotating the crystal, visit https://github.com/seto77/ReciPro/.

to individual programs. A crystal database function with over 20 000 built-in crystal structures is also implemented, and the user can immediately search and select a crystal model from the database.

Fig. 1(*a*) shows the main window of *ReciPro*. At the initial launch, several dozen crystal structures are listed in the upper part of the window. In this panel, users can select a crystal model of interest. Detailed crystallographic information regarding the selected crystal structure, such as lattice parameters, space group, atomic positions, atomic displacement parameters (Debye–Waller factors) and reference information, is shown in the lower panel. *ReciPro* supports 530 space-group notations, namely the 230 standard settings given in Volume A of *International Tables for Crystallography* (Aroyo, 2016), termed the ITA settings, and an additional 300 settings that represent non-standard axis settings (Hall, 1984). Users can import crystal structures from a crystallographic information file (CIF) or the built-in crystal structure database. Any changes to the list are automatically saved and loaded during the next launch.

The orientation of a crystal model can be specified by the Euler angles Φ, Θ and Ψ, zone axis indices, or lattice plane indices, which can also be freely rotated with the mouse and/or arrow keys in the left-hand panel. The various above-mentioned crystallographic functions (subroutines), which will be introduced in detail in the following sections, can be launched by icons lined up vertically in the right-hand panel. *ReciPro* is not merely a patchwork of the features found in existing software and libraries. Most of the implemented functions have been programmed for multi-threading parallelization, and a modern many-core CPU allows high-performance calculations; all functions can be performed synchronously. For example, if we rotate the crystal model, the corresponding 3D crystal structure image, stereographic projection, single-crystal diffraction pattern and HRTEM image in their individual functional windows are immediately

redrawn almost in real time, as shown in Fig. 1(*b*) and online (https://github.com/seto77/ReciPro/).

Currently, *ReciPro* is continuously well maintained by the developer and the features are frequently improved and/or extended. The first version (Version 1.00) was developed in 2002, and the latest version at the time of writing this article is 4.828 with many improvements and extensions. Although only the compiled executable file was distributed free of charge before Version 4.741, the more recent versions are open source.

3. Crystal database

The built-in crystal database in *ReciPro* contains over 20 000 crystal structure models provided by the American Mineralogist Crystal Database (AMCSD) (Downs & Hall-Wallace, 2003). The AMCSD includes every structure published in *American Mineralogist*, *The Canadian Mineralogist*, the *European Journal of Mineralogy* and *Physics and Chemistry of Minerals*, as well as selected data sets from other journals. In *ReciPro*, the database is highly compressed ($\sim$9 MB) and included in the installation file, and it is therefore available in an offline environment (such as an isolated laboratory). As shown in Fig. 2, users can search crystal structures from the database using various options (crystal name, contained elements, symmetry and density) and can add the identified crystal structures to the list in the main window. When publishing results using crystal structures obtained from this database, researchers are requested to include citations for Downs & Hall-Wallace (2003) and for the reference in which the structure was analysed.

4. Rotation geometry

ReciPro uses a right-handed Cartesian coordinate system, where the X axis is defined as the rightwards direction on the screen (PC monitor), the Y axis as the upwards direction on

Figure 2
The user interface for the Crystal Database
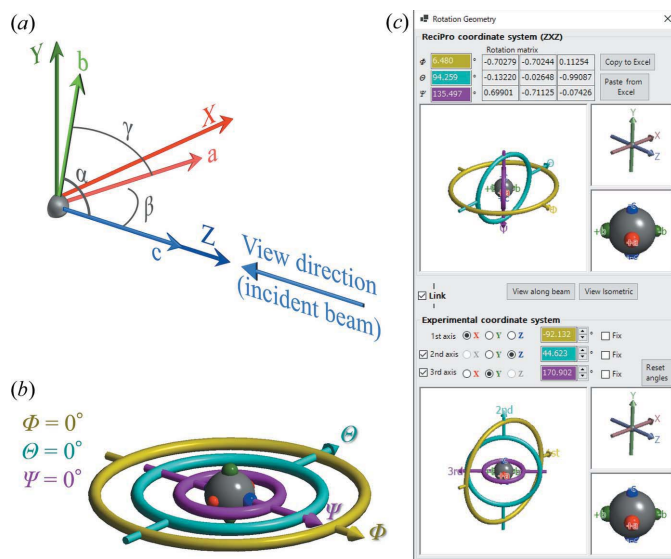
Figure 3
(*a*) Definitions of the coordinate system and initial crystal orientation, and (*b*) definitions of the Euler angles in *ReciPro*. (*c*) The user interface for Rotation Geometry.

Figure 4
The user interface for the Structure Viewer and examples of visualization. (*a*) $Mg_3Al_2Si_3O_{12}$ garnet with Mg—O, Si—O and Al—O bonds and SiO_4 polyhedra. (*b*) FeS_2 pyrite with {201} and {100} surfaces. (*c*) Fe_3O_4 magnetite with {220} lattice planes.

the screen and the *Z* axis as the frontwards direction perpendicular to the screen [Fig. 3(*a*)]. The Euler angles Φ, Θ and Ψ are employed to represent arbitrary rotation states of a crystal. At $\Phi = \Theta = \Psi = 0$, the rotation axes corresponding to Φ, Θ and Ψ coincide with the *Z*, *X* and *Z* axes, respectively (*Z*–*X*–*Z* setting) [Fig. 3(*b*)]. The initial crystal orientation (*i.e.* $\Phi = \Theta = \Psi = 0$) is defined as follows: (i) the *c* axis coincides with the *Z*-axis direction and (ii) the *b* axis lies on the *YZ* plane and is close to the *Y* axis [Fig. 3(*a*)]. In other words, the [001] axis always corresponds to the *Z* axis and the (100) plane to the *X* axis. Note that these definitions are compatible with the electron backscatter diffraction software provided by Thermo Fisher Scientific Inc. (USA).

These definitions of the rotation axes and initial crystal orientation in *ReciPro* are not necessarily applicable to actual experimental systems. The Rotation Geometry function can resolve this discrepancy [Fig. 3(*c*)]. The upper part of the GUI shows the Euler angles in *ReciPro* and the lower part has interfaces where users can set up arbitrary goniometer definitions. By linking the Euler angles in *ReciPro* to the goniometer in the laboratory, this function provides information on how the goniometer should be rotated to achieve the desired orientation (*e.g.* low-order zone axis). It will be of help to beginners who are not familiar with goniometer operations.

5. Structure viewer

ReciPro can visualize a crystal structure model as an attractive 3D graphic using an OpenGL architecture. We developed this function using the modern GLSL programming language, which allows fast and high-quality rendering of 3D objects. Even complex crystal structures containing tens of thousands of atoms can be drawn smoothly in real time. The rendered object includes constituent atoms, bonds, coordination polyhedra, unit cells, lattice planes and legend labels. Bonds are
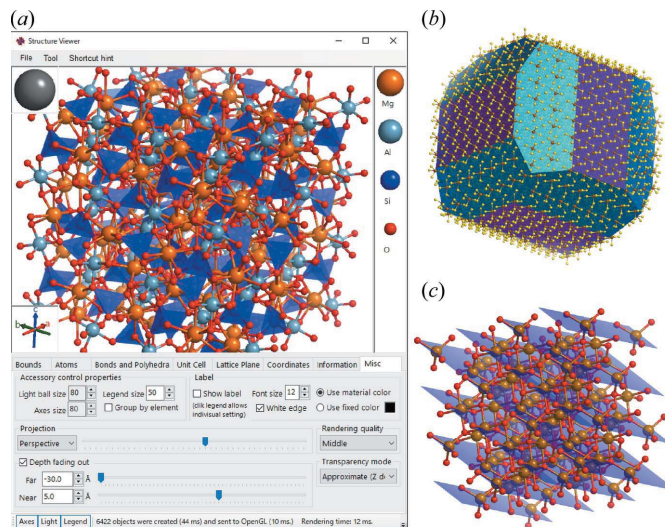
defined by specifying the shortest and longest interatomic distances, which are displayed as cylinders. Coordination polyhedra are drawn in the same colour as the central atom and are displayed translucently [Fig. 4(*a*)]. The default drawing colours and sizes of the atoms are set to be the same as those of *VESTA* (Momma & Izumi, 2011), a well known 3D visualization program for crystal structure models. The drawing range is specified by the multiple of the unit cell or by the indices of the crystal planes and their distance from the centre. By colouring the bounding plane, arbitrary crystal habits can also be represented [Fig. 4(*b*)]. Furthermore, any lattice planes [Fig. 4(*c*)] can be displayed, which will help beginners understand the concept of lattice planes in diffraction phenomena. The rotation, movement and magnification/reduction of this 3D crystal structure can be freely controlled using the mouse, and the rotation state is immediately reflected in the crystal orientation in both the main window and the other functional windows.

6. Stereonet

This function plots the directions of the crystal planes and crystal axes on a stereographic net (Fig. 5). Both equal-angle (Wulff net) and equal-area (Schmidt net) projections are supported, and the corresponding lines of latitude and longitude are also drawn. The indices of the plane or axis to be drawn can be specified by a numerical range or directly by a numerical value. The drawing objects can be saved or copied in a vector format, and so the user can change the elements (*e.g.* font and colour) later without losing resolution. From this stereographic projection image, we can easily determine the appropriate rotation angles and directions of a crystal to obtain the desired crystal orientation or diffraction condition using a goniometer on the diffractometer or microscope. In
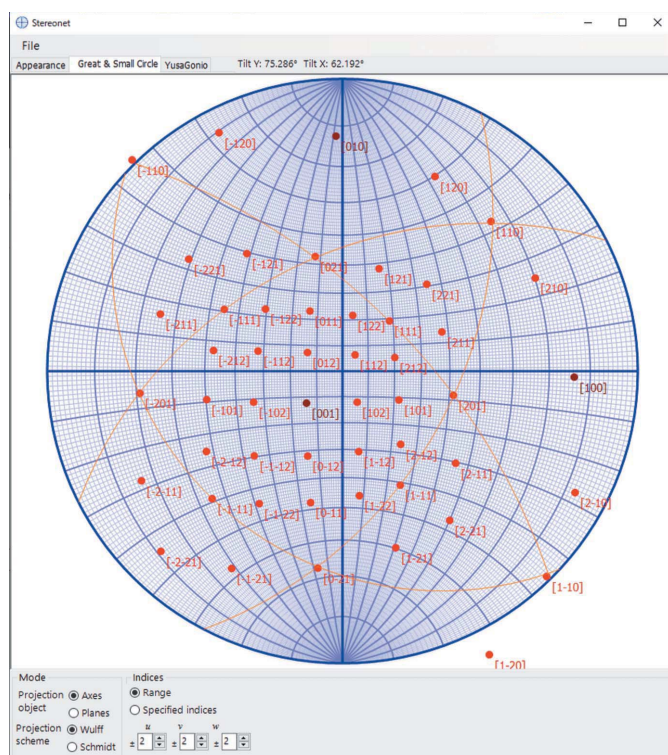
Figure 5
The user interface for Stereonet.

particular, when using a double tilting holder for TEM, the latitude and longitude directly correspond to the two tilt angles.

7. Diffraction simulator

Fig. 6 shows the GUI of the Diffraction Simulator and the simulated diffraction patterns. Various plotting options can be set using the GUI. Monochromatic X-rays, electrons and neutrons are available as incoming waves (beams) and the kinetic energy can be freely configured. The energy of the characteristic X-rays for $_1H$ to $_{98}Cf$ (Chantler, 1995) is built in. The plotting range of the simulated diffraction pattern is specified by the image resolution (*i.e.* pixel size) and the distance between the sample and detector (*i.e.* camera length). Cases in which the detector is not perpendicular (tilted) to the incident beam are also supported. The crystal rotation (*i.e.* diffraction condition) can be controlled in this window and can be immediately synchronized with the other windows.

Although the Diffraction Simulator is mainly designed for diffraction pattern simulation obtained from a single-crystal sample, as shown in Fig. 6(*a*), it also supports simulation of a Debye ring pattern assuming a polycrystalline sample with a uniform orientation distribution in all directions [Fig. 6(*b*)]. In the Debye ring simulation, the kinematic scattering approximation is applied to any incoming wave.

7.1. Kinematic simulations of X-ray, electron and neutron diffraction

The diffraction patterns of a single crystal obtained with a collimated parallel incident beam of X-rays, electrons or
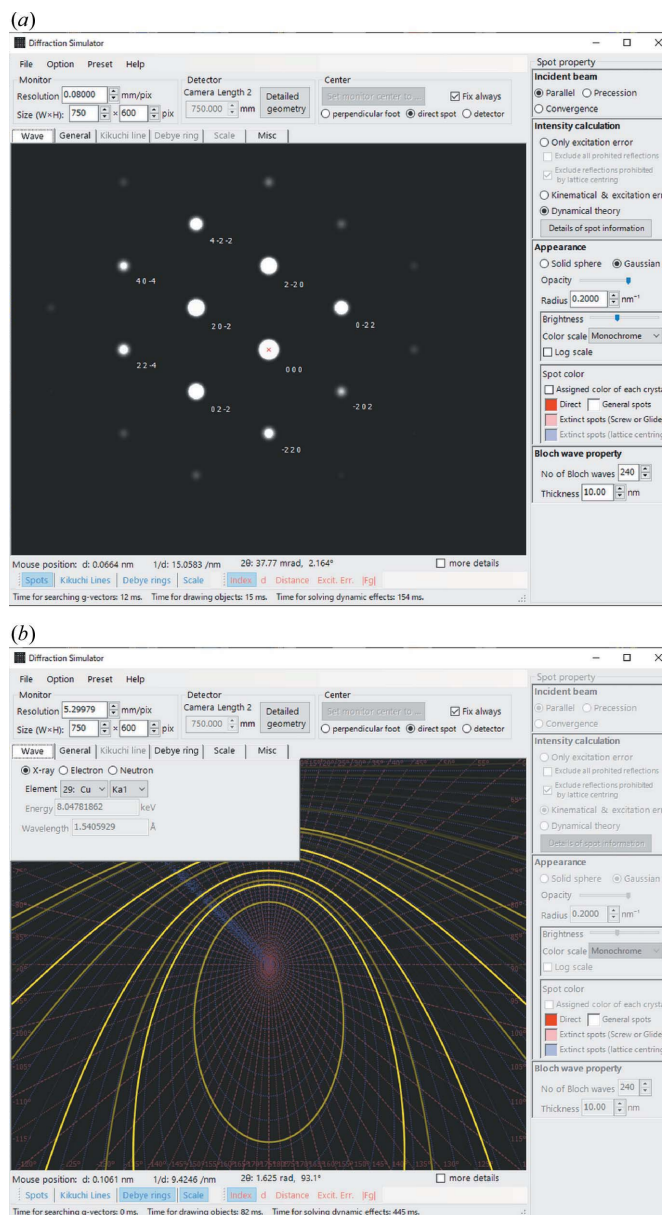
Figure 6
The user interface for the Diffraction Simulator and simulated patterns. (*a*) An electron diffraction pattern for a single crystal of silicon from a direction 0.5° off [111]. (*b*) An X-ray diffraction pattern for polycrystalline Al_2O_3 when the detector is tilted at 45° to the incident beam.

neutrons can be calculated using the kinematic scattering approximation (*i.e.* single scattering approximation). The diffraction intensities are simply estimated from the square of the crystal structure factor amplitude and excitation error (distance between the Ewald sphere and the reciprocal-lattice point). Specifically, the reciprocal-lattice point is considered as a sphere with a volume proportional to the amplitude or as a 3D Gaussian function whose integral value is the amplitude, instead of the actual spreading of a reciprocal-lattice point owing to the shape factor related to the sample shape, and the cross section of the sphere or 3D Gaussian function by the Ewald sphere is displayed. Thus, the diffraction spots are shown as circles or 2D Gaussian intensity distributions. The

crystal structure factors are calculated from the superposition of atomic scattering factors or bound coherent scattering lengths parameterized for various neutral atoms or ions. The atomic scattering factors for X-rays are calculated from linear combinations of the parameterized Gaussian functions tabulated by Waasmaier & Kirfel (1995). The atomic scattering factors for electrons are also calculated using Gaussian-type parametrizations tabulated by Peng et al. (1996) and Peng (1998). The bound coherent scattering lengths (b_c) for neutrons are taken from Table 4.4.4.1 in *International Tables for Crystallography*, Volume C (Prince, 2004). The effect of attenuation on the diffraction intensities due to isotropic or anisotropic atomic displacement factors is also incorporated.

7.2. Dynamical simulations of electron diffraction patterns

The dynamical scattering simulations of parallel-beam electron diffraction [selected-area electron diffraction (SAED) in experimental geometry], precession electron diffraction (PED) and convergent-beam electron diffraction (CBED), based on the Bloch-wave method (Bethe, 1928), are also supported by *ReciPro*. Recent reviews of the Bloch-wave method are provided by Fultz & Howe (2013), Zuo & Spence (2017) and Kirkland (2020), and some details are also explained briefly in Appendices *A*, *B* and *D*.

In the parallel-beam mode for SAED and precession mode for PED pattern simulations, the diffracted intensities of individual Bragg reflections are shown in the display area of the Diffraction Simulator window, with the size of the circles or the width of the 2D Gaussian distributions similar to the X-ray and neutron diffraction patterns, as shown in Figs. 7(*a*) and 7(*b*). The diffracted intensities on an SAED pattern are simply calculated for parallel-beam illumination (*i.e.* plane wave) incident along a specified zone axis of a crystal model. In contrast, a PED pattern is calculated from the summation over a series of SAED patterns in which the direct beam positions are aligned to the same position, obtained with tilted incident beams, because PED patterns are experimentally obtained with the rotation of a tilted nearly parallel electron beam around the optical axis of a transmission electron microscope and the subsequent compensation of the displacement of the incident beam from the optical axis by deflection coils below the sample. In a PED simulation, users should specify not only the polar tilting angle from the optical

axis but also the azimuthal angular resolution of the rotation of the tilted beam, because the azimuthal tilting angle of the incident beam is discretely sampled to reproduce beam rotation accurately. The PED technique is regarded as drastically reducing the dynamical scattering effect on electron diffraction patterns and potentially enables us to solve a crystal structure from a diffraction pattern similar to X-ray and neutron diffraction in a more straightforward manner (Vincent & Midgley, 1994; Midgley & Eggeman, 2015). This PED simulation function can be applied to, for example, a simple crystal structure analysis by comparing experimental and simulated PED patterns, and also to the optimization of PED experimental conditions to satisfy sufficiently the quasi-kinematic condition.

In the convergent-beam mode for CBED pattern simulations, an incident convergent electron beam is expressed by the superposition of numerous partial incident plane waves accepted inside the condenser aperture, which defines the incident-beam convergence semi-angle (corresponding to the diffracted disc size). The region inside the condenser aperture is discretely sampled on a uniform grid according to a user-specified division number, as shown in Fig. 7(*c*), and a set of SAED patterns obtained with the partial incident plane-wave beams corresponding to the sampled incident directions are calculated (Zuo & Spence, 2017). Individual simulated SAED patterns are arranged on the diffraction plane with the appropriate position corresponding to the partial incident-beam tilting angles, and appropriate image interpolation is applied to fit the screen resolution. The brightness of individual pixels in the display region directly expresses the diffracted intensity, as shown in Fig. 7(*c*). Furthermore, in this CBED simulator, we can simultaneously calculate CBED patterns for different thicknesses and interactively change the displayed pattern. This function is very useful for determining the sample thickness by comparing an experimental CBED pattern with the corresponding through-thickness simulation (Buxton et al., 1976; Williams & Carter, 2009; Carter & Williams, 2016). In the current version of *ReciPro*, phase interference in the overlapping region of CBED discs obtained by increasing the incident-beam convergence semi-angle is not considered; thus, the calculated CBED patterns are equivalent to an incoherent CBED pattern obtained using a low-coherence electron source or a position-averaged CBED pattern obtained with probe scanning.

In all the above simulations, users should prepare appropriate plane-wave basis sets consisting of not only zeroth-order Laue zone (ZOLZ) reflections but also lower- and higher-order Laue zone reflections to represent sufficiently exact Bloch waves. *ReciPro* can automatically select significant plane-wave components (*i.e.* strong diffracted beams) on the basis of two beam-selection criteria: (i) the number of beams specified by the user and (ii) the significance of the beams. The significance of individual beams is evaluated by the function $R = \mathbf{g}^2|Q_g|$, where $Q_g = \mathbf{k}^2 - (\mathbf{k} + \mathbf{g})^2 = 2[(\mathbf{k} + \mathbf{g}) \cdot \mathbf{s}_g + s_g^2/2]$ is a quantity related to the excitation error $\mathbf{s}_g$, and $\mathbf{k}$ and $\mathbf{g}$ are the wavevectors of the incident electron beam and the reciprocal-lattice vector, respectively. Here, $\mathbf{s}_g$ is defined as the
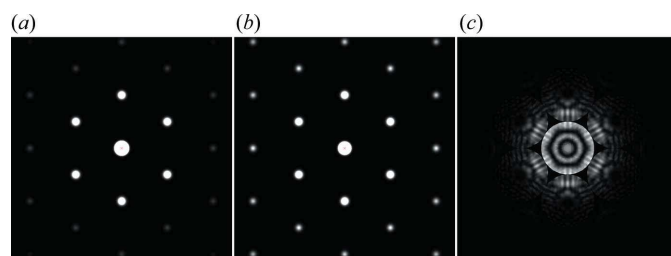
Figure 7
Simulated electron diffraction patterns of silicon [111] with 200 nm thickness. (*a*) SAED, (*b*) PED with a precession angle of 50 mrad and (*c*) CBED with a semi-angle of 6.5 mrad. All diffraction patterns were calculated with 512 beams to obtain sufficiently converged results.

deviation vector parallel to the Z direction [Fig. 3(a)] from a reciprocal-lattice point **g** to the corresponding Ewald sphere surface point. A smaller R value indicates that the beam is expected to be strong, and beams will be selected in ascending order of R values up to the user-defined number of beams.

Note that we have implemented the Bloch-wave method to select crystal orientations flexibly in *ReciPro*. Although this scheme has a considerably lower computational efficiency than the fast Fourier transform (FFT)-based multislice method, the FFT multislice calculation requires a 2D periodicity along the directions perpendicular to the electron propagation direction. Consequently, the available crystal orientation is frequently limited within some low-order zone axis orientations, and the Bloch-wave scheme was chosen to avoid this limitation.

To overcome or reduce the above-mentioned high computational costs, several features have been implemented. For example, two approaches are available for Bloch-wave calculations: (i) A classical scattering matrix method (Fujimoto, 1959; Sturkey, 1962; Yamazaki *et al.*, 2013), sometimes called the stacked Bloch-wave method (Pennington *et al.*, 2014), can be used to calculate the matrix exponentials directly using the scaling and squaring method with the Padé approximation (Higham, 2005). (ii) The Bethe eigenvalue method, which uses matrix diagonalizations to obtain the eigenvalues and eigenvectors of individual Bloch eigenstates directly, can be used instead. The fastest of these algorithms will be automatically selected. The scattering matrix method is also briefly explained in Appendix *C*. In both methods, the best mathematical library for matrix and vector operations is also automatically selected from *Eigen* (https://eigen.tuxfamily.org), *Intel MKL* (https://software.intel.com/mkl) and *Math.NET* (https://mathdotnet.com/), depending on the capabilities of the user's computer system and the simulated pattern (SAED, PED or CBED).

The computational cost of the potential calculation part before the calculation of the dynamical scattering process has also been reduced. *ReciPro* considers only the imaginary parts of the crystal potential that describe the phenomenological absorption of elastically scattered electrons due to thermal diffuse scattering (TDS), which is the most dominant inelastic scattering related to phonon excitations (Hall & Hirsch, 1965; Bird & King, 1990; Weickenmeier & Kohl, 1991). This is calculated analytically instead of by time-consuming numerical integration (Kuramochi, 2009; Ohtsuka, 2013). Note that this speed-up scheme assumes both the projection approximation (*i.e.* a flat Ewald sphere as a high-energy approximation) and atomic scattering factors approximated by the superposition of Gaussian functions (Peng *et al.*, 1996; Peng, 1998).

8. HRTEM simulator

In the latest version of *ReciPro*, HRTEM image simulation is also implemented using the same theoretical framework as the dynamical simulation function in the Diffraction Simulator. It is well known that the image contrast of HRTEM images is not

a direct projection of the atomic arrangement because it is strongly modulated by lens aberrations of the objective lens, such as the spherical aberration and defocus value, and by the partial spatial and temporal coherences of the electron beam, as well as the variation in sample thickness due to the dynamical scattering effect. To determine the atomic arrangement from an HRTEM image, we quantitatively compare the experimental image and the precise simulations while considering such effects. In *ReciPro*, two types of imaging model handling partial coherence are considered: (i) the linear contrast transfer theory, in which the partial coherence is considered by simple convolution between the outgoing waves from a sample and the envelope function accompanied by the contrast transfer function describing the lens aberrations, and (ii) the nonlinear contrast transfer theory based on a more accurate first-order transmission cross coefficient (Ishizuka, 1980). The details of these models are briefly explained in Appendix *E*. Although the former model has a lower computational cost than the latter, the linear contrast transfer theory tends to break down for thicker samples in which the weak phase object approximation is not satisfied. The latter model is a more reliable option, even for thicker samples and/or higher atomic number (Z) materials. Furthermore, a random deflection of the image relative to the detector due to factors such as sample drift, instability of the lens current, thermal magnetic noise and the modulation transfer function of the detectors can be approximated as the Gaussian blurring of HRTEM images to overcome or reduce the Stobbs factor (Hÿtch & Stobbs, 1994; Thust, 2009).

Fig. 8 shows the HRTEM Simulator window. The optical parameters of the electron microscope (such as the acceleration voltage, spherical aberration coefficient, defocus value and sample thickness) can be set through the GUI on the right-hand panel of the window. The simulated images are displayed in the left-hand panel of the window. Users can
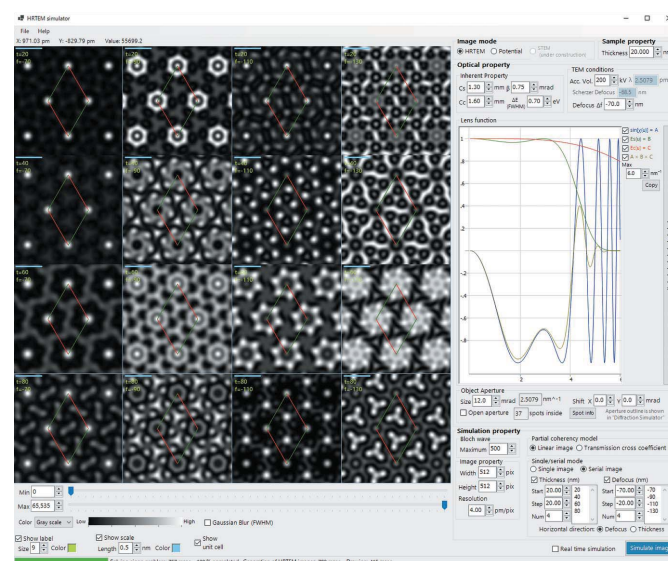
Figure 8
The user interface for the HRTEM Simulator. Simulated images were obtained for hexagonal Si_3N_4.

change the size and position of the objective lens aperture and check these in the Diffraction Simulator window (Fig. 6). The contrast transfer function describing the lens aberrations, accompanied by the envelope function representing the partial coherence effect within the linear contrast transfer theory for a specified optical condition, can be plotted in the right-hand panel. The HRTEM image series can be simultaneously calculated with a variation in the sample thickness and defocus value.

In the near future, a Bloch-wave-based STEM image simulation feature based on the absorptive potential model (Pennycook & Jesson, 1991; Watanabe *et al.*, 2001; Ishizuka, 2002; Allen *et al.*, 2003) will be implemented in this function.

9. Spot ID

There are two versions of Spot ID, both of which provide functions for analysing real SAED patterns. Spot ID v1 has a simple function to search zone axes using the geometric configuration of diffraction spots (in ZOLZ) arranged in a 2D lattice [Fig. 9(*a*)]. Although it is necessary to measure manually the distances and angles between the spots from the SAED images, candidates for the zone axis are immediately

displayed once these values are entered. We can also analyse two or three images simultaneously and, if we input the angle condition of the holder when the images are acquired, analysis becomes more accurate.

Spot ID v2, in contrast, starts by importing the image data of the SAED pattern itself [Fig. 9(*b*)]. It can import numerous image formats widely employed in the TEM community, such as the standard 32-bit tagged image file format (`.tif`), and the Digital Micrograph 3 and 4 (`.dm3` and `.dm4`) formats produced by Gatan Inc. (USA). The diffracted spots in the loaded image are automatically detected and fitted with an appropriate 2D bell-shaped function (2D pseudo-Voigt function). Next, the position of the reciprocal-lattice vector (**g**) corresponding to each diffraction spot is calculated on the basis of information such as the image resolution, camera length and electron energy. Finally, for the crystal structure selected in the main window, an exhaustive search is performed for orientations that satisfy the arrangement of the reciprocal-lattice vectors. This algorithm even allows the accurate determination of high-order zone axes.

10. Software availability

ReciPro is a completely free program distributed under the MIT licence and runs on the Microsoft Windows 7, Windows 8.1 and Windows 10 (and probably Windows 11) operating systems with the Microsoft .NET Desktop Runtime 6.0. *ReciPro* is installed by downloading and executing the setup file (`ReciProSetup.msi`) on the project's GitHub page, https://github.com/seto77/ReciPro/releases/latest. All source code is written in C++, C# and GLSL languages and published in the above GitHub repository as a *Visual Studio 2022* project. Detailed documentation on how to use the software is also available at https://github.com/seto77/ReciPro/raw/master/ReciPro/doc/ReciProManual(en).pdf.

11. Conclusions

In summary, *ReciPro* is a free open-source GUI-based multi-purpose crystallography program that supports crystallographers at all levels, from beginner to advanced. By simply installing the software, users can seamlessly access several features, such as the built-in crystal database containing over 20 000 crystal models, a visualization system for crystal structures, a quantitative diffraction simulator, stereographic projection of crystal planes/axes and a semi-automatic diffraction spot indexing function. In addition, there are several other functions that have not been introduced in this paper. *ReciPro* is a program subject to ongoing development and it is regularly updated with new features and bug fixes. Please report bugs, requests or comments on the above GitHub issue page.

APPENDIX *A*
Bloch-wave method

According to Bloch's theorem, inside a crystalline material consisting of a periodic crystal potential $V(\mathbf{r})$, the eigenstate of

Figure 9
The user interfaces for (*a*) Spot ID v1 and (*b*) Spot ID v2.

incident electrons associated with an eigenwavevector $\mathbf{k}$ takes the form of a Bloch wave,

$$b(\mathbf{k}, \mathbf{r}) = \sum_g C_g(\mathbf{k}) \exp[2\pi i(\mathbf{k} + \mathbf{g}) \cdot \mathbf{r}], \qquad (1)$$

where the Bloch wave has been expanded to the plane-wave basis set in terms of the reciprocal-lattice vector $\mathbf{g}$ and C_g is the expansion coefficient (Fourier coefficient). Therefore, the general solution of the wavefunction of the incident electrons is the linear superposition of the eigenstates $b(\mathbf{k}, \mathbf{r})$,

$$
\begin{aligned}
\psi(\mathbf{r}) &= \sum_j \alpha^{(j)} b(\mathbf{k}^{(j)}, \mathbf{r}) \\
&= \sum_j \alpha^{(j)} \sum_g C_g^{(j)}(\mathbf{k}^{(j)}) \exp\left[2\pi i(\mathbf{k}^{(j)} + \mathbf{g}) \cdot \mathbf{r}\right], \qquad (2)
\end{aligned}
$$

where the superscript j denotes the jth Bloch wave and $\alpha^{(j)}$ is the excitation amplitude of the Bloch wave.

The periodic crystal potential can also be expanded into a Fourier series:

$$V(\mathbf{r}) = -\frac{h^2}{2m} U(\mathbf{r}) = -\frac{h^2}{2m} \sum_g (U_g + iU_g') \exp(2\pi i\mathbf{g} \cdot \mathbf{r}), \quad (3)$$

where h is the Planck constant, $m = \gamma m_0$ is the electron relativistic mass, and γ and m_0 are the relativistic correction factor and the electron rest mass, respectively. The crystal potential should be a complex optical potential instead of a mere Coulomb potential. The real part of the scaled optical potential $U(\mathbf{r})$ describes the elastic scattering contribution due to the Coulomb interaction between the incident electrons and the crystal, and the imaginary part incorporates the inelastic scattering contribution as the phenomenological absorption of elastically scattered electrons (Yoshioka, 1957). Therefore, U_g and U_g' are the Fourier coefficients of the Coulomb potential and absorption potential, respectively. In *ReciPro*, only the contribution of TDS related to phonon excitations, which is the most dominant inelastic scattering event, is included in the absorption potential.

In the dynamical electron scattering theory, we need to know the eigenwavevectors $\mathbf{k}^{(j)}$ that are physically allowed inside a crystal when the incident electrons have a particular kinetic energy E in a vacuum, related to the acceleration voltage of an electron microscope. Individual eigenstates (Bloch waves) can be obtained by solving the time-independent one-body Schrödinger equation,

$$\left[-\frac{\hbar^2}{2m} \nabla^2 + V(\mathbf{r})\right] b(\mathbf{k}^{(j)}, \mathbf{r}) = Eb(\mathbf{k}^{(j)}, \mathbf{r}), \qquad (4)$$

where $\hbar$ is the reduced Planck constant. This Schrödinger equation can be rewritten using the scaled optical potential as follows:

$$\left\{\nabla^2 + 4\pi^2\left[k_{\text{vac}}^2 + U(\mathbf{r})\right]\right\} b(\mathbf{k}^{(j)}, \mathbf{r}) = 0, \qquad (5)$$

where $\mathbf{k}_{\text{vac}}$ is the wavevector of incident electrons in a vacuum, which satisfies the relation $E = h^2 k_{\text{vac}}^2/2m$. By substituting equations (1) and (3) into equation (5), we arrive at the starting equation of the Bloch-wave method (Bethe, 1928),

$$\left[k_0^2 - \left(\mathbf{k}^{(j)} + \mathbf{g}\right)^2 + iU_0'\right] C_g^{(j)}(\mathbf{k}^{(j)})$$
$$+ \sum_{h \neq g} \left(U_{g-h} + iU_{g-h}'\right) C_h^{(j)}(\mathbf{k}^{(j)}) = 0, \qquad (6)$$

where $k_0^2 = k_{\text{vac}}^2 + U_0$, and U_0 is the mean inner crystal potential.

The boundary condition at the entrance surface of a crystalline sample requires the tangential components $\mathbf{k}_{\text{vac}}$ and $\mathbf{k}^{(j)}$ to be identical. This means that the refraction effect due to the mean inner crystal potential U_0 included in $\mathbf{k}_0$ should modulate only the longitudinal components of $\mathbf{k}_{\text{vac}}$ as $\mathbf{k}_0 \simeq \mathbf{k}_{\text{vac}} + [U_0/2(\mathbf{k}_{\text{vac}} \cdot \mathbf{n}) \cdot \mathbf{n}$, and $\mathbf{k}^{(j)}$ may also be decomposed as follows:

$$\mathbf{k}^{(j)} = \mathbf{k}_0 + \lambda^{(j)}\mathbf{n} = \mathbf{k}_0 + \left(\gamma^{(j)} + i\eta^{(j)}\right)\mathbf{n}, \qquad (7)$$

where $\lambda^{(j)}$ is the complex eigenvalue, the real part $\gamma^{(j)}$ is the *anpassung* and the imaginary part $\eta^{(j)}$ is the absorption coefficient. $\mathbf{n}$ is the unit vector normal to the entrance surface directed into the crystal. The geometric relationships between $\mathbf{k}_0$, $\mathbf{k}_{\text{vac}}$, $\mathbf{k}^{(j)}$, $\mathbf{g}$ and $\gamma^{(j)}$ are shown in Fig. 10.

Substituting equation (7) into equation (6), we can rewrite the inside of the bracket in equation (6) as follows:

$$k_0^2 - \left(\mathbf{k}^{(j)} + \mathbf{g}\right)^2 + iU_0' = -\left(\lambda^{(j)}\right)^2 - \lambda^{(j)} P_g + Q_g + iU_0', \qquad (8)$$

where $P_g = 2\mathbf{n} \cdot (\mathbf{k}_0 + \mathbf{g})$ and $Q_g = -\mathbf{g} \cdot (2\mathbf{k}_0 + \mathbf{g})$. In the geometry of high-energy electron diffraction, the quadratic term $(\lambda^{(j)})^2$ can be negligible because this term is usually very small compared with k_0 (Kim & Sheinin, 1982), and therefore equation (6) can be reduced to

$$\left(Q_g + iU_0'\right) C_g^{(j)}(\mathbf{k}^{(j)}) + \sum_{h \neq g} U_{g-h} C_g^{(j)}(\mathbf{k}^{(j)}) = \lambda^{(j)} P_g C_g^{(j)}(\mathbf{k}^{(j)}). \quad (9)$$

In matrix notation, this can be expressed as the following generalized linear eigenvalue problem, in which a set of $\lambda^{(j)}$ and $C_g^{(j)}$ are the eigenvalue and the eigenvector, respectively, as follows:

Figure 10
The geometric relationship between the incident beam, diffracted beam and reciprocal-lattice vectors inside a crystalline material. Bold and regular letters represent vectors and scalars, respectively.

$$
\mathbf{A} \begin{pmatrix} C_0^{(j)} \\ C_g^{(j)} \\ C_h^{(j)} \\ \vdots \end{pmatrix} = \lambda^{(j)} \begin{pmatrix} C_0^{(j)} \\ C_g^{(j)} \\ C_h^{(j)} \\ \vdots \end{pmatrix}. \tag{10}
$$

Here the matrix elements $\{\mathbf{A}\}_{g,h} = [(Q_g + iU_0')/P_g]\delta_{g,h} + [(U_{g-h} + iU_{g-h}')/P_g](1 - \delta_{g,h})$ and $\delta_{i,j}$ is the Kronecker delta function. Furthermore, we can rewrite this matrix equation as $\mathbf{A} \cdot \mathbf{C} = \mathbf{C} \cdot \mathbf{\Lambda}$, where $\{\mathbf{C}\}_{g,j} = C_g^{(j)}$ and $\{\mathbf{\Lambda}\}_{i,j} = \lambda^{(j)}\delta_{i,j}$. By solving this eigenvalue problem, we can obtain n sets of Bloch-wave solutions allowed inside the crystal for incident electrons with kinetic energy E in a vacuum for the case in which we have expanded a Bloch wave into n plane-wave components.

APPENDIX *B*
Determination of Bloch-wave excitation amplitudes and transmission coefficients

Assuming that the sample has a flat plate shape, we decompose the position vector $\mathbf{r}$ into $\mathbf{R}$ (the projection of $\mathbf{r}$ onto the sample surface) and z (the component of $\mathbf{r}$ along the normal direction to the sample surface), that is, $\mathbf{r} = \mathbf{R} + z\mathbf{n}$. In the same manner, we also decompose the wavevector $\mathbf{k}$ as $\mathbf{k} = \mathbf{K} + k_z\mathbf{n}$, and the reciprocal-lattice vector $\mathbf{g}$ as $\mathbf{g} = \mathbf{G} + g_z\mathbf{n}$. Using these notations and summarizing equations (2) and (7), the wavefunction of the incident electrons may be rewritten as

$$
\psi(\mathbf{R}, z) = \sum_g \left\{ \sum_j \alpha^{(j)} C_g^{(j)} \exp\left[2\pi i\left(k_{0_z} + \lambda^{(j)} + g_z\right)z\right] \right\} \\ \times \exp[2\pi i(\mathbf{K} + \mathbf{G}) \cdot \mathbf{R}]. \tag{11}
$$

By applying the two-dimensional Fourier transform with respect to R, this wavefunction can be rewritten as

$$
\psi(\mathbf{Q}, z) = \sum_g \left\{ \sum_j \alpha^{(j)} C_g^{(j)} \exp\left[2\pi i\left(k_{0_z} + \lambda^{(j)} + g_z\right)z\right] \right\} \\ \times \delta(\mathbf{Q} - \mathbf{K} - \mathbf{G}), \tag{12}
$$

where $\mathbf{Q}$ is the two-dimensional spatial frequency and $\delta(\mathbf{Q})$ is the Dirac delta function. In matrix notation, the nonzero Fourier coefficients are represented as

$$
\begin{pmatrix} \psi(\mathbf{K}, z) \\ \psi(\mathbf{K} + \mathbf{G}, z) \\ \psi(\mathbf{K} + \mathbf{H}, z) \\ \vdots \end{pmatrix} = \exp\left(2\pi i k_{0_z} z\right) \mathbf{Z}(z) \cdot \mathbf{C} \cdot \exp(2\pi i \mathbf{\Lambda} z) \cdot \begin{pmatrix} \alpha^{(1)} \\ \alpha^{(2)} \\ \alpha^{(3)} \\ \vdots \end{pmatrix}, \tag{13}
$$

where $\{\mathbf{Z}(z)\}_{g,h} = \exp(2\pi i g_z z)\delta_{g,h}$ and $\{\exp(2\pi i \mathbf{\Lambda} z)\}_{i,j} = \exp(2\pi i \lambda^{(j)} z)\delta_{i,j}$.

Here, a plane-wave illumination is assumed, in which the wavefunction of incident electrons in a vacuum $\phi(\mathbf{R}, z)$ takes the form of a single plane wave,

$$
\phi(\mathbf{R}, z) = \exp(2\pi i \mathbf{k}_{\mathrm{vac}} \cdot \mathbf{r}) = \exp\left(2\pi i k_{\mathrm{vac}_z} z\right) \exp(2\pi i \mathbf{K} \cdot \mathbf{R}), \tag{14}
$$

where it is noted that $\mathbf{K} = \mathbf{K}_{\mathrm{vac}}$. Using the same matrix notation as equation (13), this equation may be rewritten as

$$
\begin{pmatrix} \phi(\mathbf{K}, z) \\ \phi(\mathbf{K} + \mathbf{G}, z) \\ \phi(\mathbf{K} + \mathbf{H}, z) \\ \vdots \end{pmatrix} = \exp\left(2\pi i k_{\mathrm{vac}_z} z\right) \begin{pmatrix} 1 \\ 0 \\ 0 \\ \vdots \end{pmatrix}. \tag{15}
$$

The excitation amplitudes of individual Bloch waves can be determined from the boundary condition that the wavefunctions of incident electrons in a vacuum and in the crystal are continuous, $\phi(\mathbf{R}, 0) = \psi(\mathbf{R}, 0)$ or $\phi(\mathbf{Q}, 0) = \psi(\mathbf{Q}, 0)$, as follows:

$$
\begin{pmatrix} \alpha^{(1)} \\ \alpha^{(2)} \\ \alpha^{(3)} \\ \vdots \end{pmatrix} = \mathbf{C}^{-1} \cdot \begin{pmatrix} 1 \\ 0 \\ 0 \\ \vdots \end{pmatrix}, \tag{16}
$$

where we assume the depth position $z = 0$ indicates the position of the entrance surface.

In contrast, the wavefunction of the transmitted electrons emitted from the exit surface, namely the exit wavefunction $\varphi(\mathbf{R}, z)$, can also be expanded as a Fourier series:

$$
\varphi(\mathbf{R}, z) = \sum_g T_g \exp[2\pi i(\mathbf{k}_{\mathrm{vac}} + \mathbf{g}) \cdot \mathbf{r}] \\ = \sum_g T_g \exp\left[2\pi i\left(k_{\mathrm{vac}_z} + g_z\right)z\right] \exp[2\pi i(\mathbf{K} + \mathbf{G}) \cdot \mathbf{R}], \tag{17}
$$

where T_g is the transmission coefficient. Using the same matrix notation as equations (13) and (15), this equation can be rewritten as

$$
\begin{pmatrix} \varphi(\mathbf{K}, z) \\ \varphi(\mathbf{K} + \mathbf{G}, z) \\ \varphi(\mathbf{K} + \mathbf{H}, z) \\ \vdots \end{pmatrix} = \exp\left(2\pi i k_{0_z} z\right) \mathbf{Z}(z) \cdot \begin{pmatrix} T_0 \\ T_g \\ T_h \\ \vdots \end{pmatrix}. \tag{18}
$$

The transmission coefficients can also be determined from the boundary condition $\psi(\mathbf{R}, t) = \varphi(\mathbf{R}, t)$ or $\psi(\mathbf{Q}, t) = \varphi(\mathbf{Q}, t)$, as follows:

$$
\begin{pmatrix} T_0 \\ T_g \\ T_h \\ \vdots \end{pmatrix} = \exp\left[2\pi i\left(k_{0_z} - k_{\mathrm{vac}_z}\right)t\right] \mathbf{C} \cdot \exp(2\pi i \mathbf{\Lambda} t) \cdot \mathbf{C}^{-1} \cdot \begin{pmatrix} 1 \\ 0 \\ 0 \\ \vdots \end{pmatrix}, \tag{19}
$$

where $z = t$ is the depth position of the exit surface.

APPENDIX *C*
Scattering matrix method

Taking a Taylor series of $\exp(2\pi i \mathbf{\Lambda} t)$, equation (19) can be rewritten as

$$\begin{pmatrix} T_0 \\ T_g \\ T_h \\ \vdots \end{pmatrix} =$$

$$\exp\Big[2\pi i\Big(k_{0_z} - k_{\mathrm{vac}_z}\Big)t\Big]\mathbf{C}\cdot\left[\sum_{n=1}^{\infty}\frac{(2\pi it)^n}{n!}\,\mathbf{\Lambda}^n\right]\cdot\mathbf{C}^{-1}\cdot\begin{pmatrix}1\\0\\0\\\vdots\end{pmatrix}.$$

(20)

At the same time, we can also easily obtain the following relation from the linear eigenvalue problem in the Bloch-wave method, $\mathbf{A}\cdot\mathbf{C} = \mathbf{C}\cdot\mathbf{\Lambda}$:

$$\mathbf{A}^n = \mathbf{C}\cdot\mathbf{\Lambda}^n\cdot\mathbf{C}^{-1}, \qquad (21)$$

which allows us to obtain the following matrix exponential:

$$\begin{aligned}\exp(2\pi i\mathbf{A}t) &= \sum_{n=1}^{\infty}\frac{(2\pi it)^n}{n!}\mathbf{A}^n \\ &= \mathbf{C}\cdot\left[\sum_{n=1}^{\infty}\frac{(2\pi it)^n}{n!}\mathbf{\Lambda}^n\right]\cdot\mathbf{C}^{-1} \\ &= \mathbf{C}\cdot\exp(2\pi i\mathbf{\Lambda}t)\cdot\mathbf{C}^{-1}.\end{aligned}$$

(22)

Therefore, equation (20) may be rewritten as

$$\begin{pmatrix} T_0 \\ T_g \\ T_h \\ \vdots \end{pmatrix} = \exp\Big[2\pi i\Big(k_{0_z} - k_{\mathrm{vac}_z}\Big)t\Big]\exp(2\pi i\mathbf{A}t)\cdot\begin{pmatrix}1\\0\\0\\\vdots\end{pmatrix}.$$

(23)

This matrix exponential $\exp(2\pi i\mathbf{A}t) = \mathbf{C}\cdot\exp(2\pi i\mathbf{\Lambda}t)\cdot\mathbf{C}^{-1}$ is termed the scattering matrix (Fujimoto, 1959; Sturkey, 1962) and describes the dynamical electron scattering process during propagation inside a crystal over a distance t along the z direction. The advantage of this formulation is that we can obtain the transmission coefficients by directly solving the matrix exponential (i.e. the scattering matrix) instead of the time-consuming matrix diagonalization to obtain the eigenvalues and eigenvectors. Nevertheless, the matrix exponential of a non-diagonal matrix $\mathbf{A}$ cannot be solved analytically, so we need to re-expand the matrix exponential into a Taylor series. In *ReciPro*, the scaling and squaring method with the Padé approximation (Higham, 2005) is implemented to solve the matrix exponential instead of the Taylor series expansion to overcome the slow convergence of the Taylor series expansion. In this scheme, the scattering matrix is approximated as

$$\exp(2\pi i\mathbf{A}t) \simeq \prod_{i=1}^{n}\exp\left(\frac{2\pi i\mathbf{A}t}{n}\right) \simeq \prod_{i=1}^{n}\{\mathbf{D}_{p,q}^{-1}\cdot\mathbf{N}_{p,q}\}, \quad (24)$$

where

$$\mathbf{N}_{p,q} = \sum_{j=0}^{p}\frac{(p+q-j)!\,p!}{(p+q)!\,j!\,(p-j)!}\left(\frac{2\pi i\mathbf{A}t}{n}\right)^j \quad (25)$$

and

$$\mathbf{D}_{p,q} = \sum_{j=0}^{q}\frac{(p+q-j)!\,q!}{(p+q)!\,j!\,(q-j)!}\left(-\frac{2\pi i\mathbf{A}t}{n}\right)^j, \quad (26)$$

In the scaling and squaring method, the parameter n corresponds to the division number of a sample of thickness t into n thin slabs, and the matrix exponential for a thin slab is expanded as equations (25) and (26) within the (p, q)-order Padé approximation. In *ReciPro*'s implementation, the parameters n, p and q are automatically set appropriately according to the L1 norm value of the scattering matrix.

Although this scattering matrix method based on the direct calculation of a matrix exponential has a significantly higher computational efficiency than the matrix diagonalization scheme, the latter technique has the advantage that the transmission coefficients for an arbitrary sample thickness can be obtained by simple matrix multiplications after the eigenvalues and eigenvectors have been computed. Therefore, the matrix diagonalization method is suitable for cases in which one wants to change the sample thickness later, while the scattering matrix method is suitable for cases in which one wants to calculate quickly only for a specific sample thickness. *ReciPro* supports both approaches and the user can select a preferred approach depending on the situation.

APPENDIX D
Crystal potential

The Fourier coefficient U_g of the crystal Coulomb potential (including the relativistic correction) is approximately given as the superposition of the potential of isolated neutral atoms or ions in a unit cell as follows:

$$U_g = \frac{\gamma}{\Omega}\sum_{\kappa}f_\kappa(g)\exp(-2\pi i\mathbf{g}\cdot\mathbf{r}_\kappa)\exp\left(-\frac{1}{4}B_\kappa g^2\right). \quad (27)$$

The subscript κ means the κth atom in the unit cell, $\mathbf{r}_\kappa$ is the atomic position and B_κ is defined as $8\pi^2\langle u_\kappa^2\rangle$, where $\langle u_\kappa^2\rangle$ is the isotropic mean-square atomic displacement resulting from thermal vibrations. $f_\kappa(g)$ is the atomic scattering factor, which is the Fourier transform of the Coulomb potential of isolated atoms/ions. In *ReciPro*'s implementation, the atomic scattering factors are calculated from an analytical form consisting of the superposition of Gaussian functions,

$$f_\kappa(g) = \sum_i a_i\exp\left(-\frac{b_i}{4}g^2\right), \quad (28)$$

where a_i and b_i are the fitting coefficients (Peng et al., 1996; Peng, 1998; Kuramochi, 2009).

Similarly, the (relativistic) absorption potential U_g' can be expressed as

$$U_g' = \frac{\gamma}{\Omega}\sum_{\kappa}f_\kappa'(\mathbf{g})\exp(-2\pi i\mathbf{g}\cdot\mathbf{r}_\kappa)\exp\left(-\frac{1}{4}B_\kappa g^2\right), \quad (29)$$

where $f_\kappa'(\mathbf{g})$ is the absorptive form factor for the κth atom. The absorption coefficients $\eta^{(j)}$ on individual Bloch waves may be

J. Appl. Cryst. (2022). **55**, 397–410   Seto and Ohtsuka · *ReciPro* **407**

electronic reprint

obtained from the above absorption potentials, as follows (Allen & Rossouw, 1989):

$$\eta^{(j)} = \frac{\sum_g \sum_h C_g^{(j)*} U'_{g-h} C_h^{(j)}}{\sum_g P_g C_g^{(j)*} C_g^{(j)}}, \quad (30)$$

where the asterisk (*) represents the complex conjugate. Note that this is a perturbative expression to establish clearly the relation between the absorption coefficient and absorption potentials. Generally, the absorption coefficients are calculated as the imaginary part of a complex eigenvalue by directly solving a generalized eigenvalue problem that consists of complex optical potentials. Furthermore, the absorption potentials and related absorptive form factors are nonlocal quantities in the more exact form (Oxley *et al.*, 2005) and this expression is based on the local approximation.

In *ReciPro*, only the inelastic scattering contribution to phonon excitations, namely TDS, is considered by the absorption potential. Within the Einstein model and using the isotropic Debye–Waller factor, the TDS contribution to the absorptive form factor can be written as follows (Hall & Hirsch, 1965; Bird & King, 1990; Weickenmeier & Kohl, 1991):

$$f'_\kappa(\mathbf{g}) = \frac{h}{2m_0 c(1-\gamma^{-2})^{1/2}} \int f_\kappa(g) f_\kappa(|\mathbf{g}-\mathbf{q}|)$$
$$\times \left\{ 1 - \exp\left[-\frac{1}{4} B_\kappa(q^2 - \mathbf{g}\cdot\mathbf{q}) \right] \right\} d\mathbf{q}, \quad (31)$$

where c is the speed of the light. This expression assumes that the Ewald sphere surface is approximately treated as an infinite plane projected parallel to the entrance surface of the crystal, and thus the above integration is performed over the infinitely flat Ewald sphere surface. Then, if we use atomic scattering factors consisting of Gaussian functions, as shown in equation (28), the above equation becomes a simple Gaussian integral problem, which is analytically solvable without time-consuming numerical integration (Kuramochi, 2009; Ohtsuka, 2013):

$$f'_\kappa(\mathbf{g}) = \frac{2h}{m_0 c(1-\gamma^{-2})^{1/2}} \sum_i \sum_j a_i a_j$$
$$\times \left\{ \frac{\pi}{b_i + b_j} \exp\left[-\frac{b_i b_j}{4(b_i + b_j)} g^2 \right] \right.$$
$$\left. - \frac{\pi}{b_i + b_j + 2B_\kappa} \exp\left[-\frac{b_i b_j - B_\kappa^2}{4(b_i + b_j + 2B_\kappa)} g^2 \right] \right\}. \quad (32)$$

This formulation of the TDS absorptive form factor under the flat Ewald sphere approximation is a completely local quantity and the aforementioned local approximation is perfectly established (Ohtsuka *et al.*, 2013).

APPENDIX *E*
Influence of partial coherence on HRTEM images

An HRTEM image is a magnified image of the electron-density distribution on the exit surface of a sample transferred to the image plane through several projector lenses. However,

the phase distribution of the exit wavefunction is modulated owing to the lens aberrations of the objective lens. The HRTEM image $I(\mathbf{R})$ can be expressed as the squared amplitude of a simple convolution product of the exit wavefunction $\psi(\mathbf{R}, t)$ and the point spread function $t(\mathbf{R})$ as follows:

$$I(\mathbf{R}) = \left| \psi(\mathbf{R}, t) \otimes t(\mathbf{R}) \right|^2 = \left| \mathcal{F}_{\mathbf{Q}\to\mathbf{R}}^{-1}[\psi(\mathbf{Q}, t)\, t(\mathbf{Q})] \right|^2, \quad (33)$$

where the operator $\otimes$ is the convolution operation and $\mathcal{F}_{\mathbf{Q}\to\mathbf{R}}^{-1}$ is the inverse Fourier transform with respect to $\mathbf{R}$ from $\mathbf{Q}$. The reciprocal-space point spread function $t(\mathbf{Q}) = A(\mathbf{Q})\exp[-i\chi(\mathbf{Q})]$, where $A(\mathbf{Q})$ is the aperture function and $\chi(\mathbf{Q})$ is the lens aberration function. The aperture function $A(\mathbf{Q})$ describes the shape of the objective aperture,

$$A(\mathbf{Q}) = \begin{cases} 1 & \text{(inside the objective aperture)}, \\ 0 & \text{(outside the objective aperture)}. \end{cases} \quad (34)$$

The $\mathbf{Q}$-dependent phase shift $\chi(\mathbf{Q})$ due to the lens aberrations takes the form

$$\chi(\mathbf{Q}) = \pi\lambda|\mathbf{Q}|^2 \left(\Delta f + \lambda^2 C_s |\mathbf{Q}|^2/2 \right), \quad (35)$$

where λ is the wavelength of the incident electrons, Δf is the defocus value and C_s is the spherical aberration coefficient. This form incorporates up to third-order aberrations; other higher-order aberrations are neglected.

However, the formation of HRTEM images is never perfectly coherent, as in the above model, except for the ideal case in which the electron source is a perfect point source and produces perfectly monochromatic electrons and the lens system is also perfectly stabilized. In actual microscopes, we cannot avoid small instabilities in the acceleration voltage and lens current, which produce a small spread in the defocus value. Furthermore, an electron source with a finite size cannot produce ideal parallel illumination of a sample, and the actual illumination for HRTEM imaging has a finite nonzero divergence angle. The former and latter contributions decrease the temporal coherence and spatial coherence, respectively, and they introduce the concept of partial coherence into the HRTEM imaging model. In *ReciPro*, HRTEM image simulations can be carried out accompanied by partial coherence using the transmission cross coefficient (TCC) model or a more simplified linear image model.

E1. Transmission cross coefficient model

In the TCC model, the HRTEM image intensity distribution is expressed as

$$I(\mathbf{R}) = \mathcal{F}_{\mathbf{Q}-\mathbf{Q}'\to\mathbf{R}}^{-1} \left[\iint \psi(\mathbf{Q}, t)\, \psi^*(\mathbf{Q}', t)\, T_{cc}(\mathbf{Q}, \mathbf{Q}')\, d\mathbf{Q}\, d\mathbf{Q}' \right], \quad (36)$$

where $T_{cc}(\mathbf{Q}, \mathbf{Q}')$ describes the strength of pairwise interference between spatial frequency components $\mathbf{Q}$ and $\mathbf{Q}'$, and this is termed the transmission cross coefficient. In other words, T_{cc} expresses the coherence between individual direct and diffracted beams, and the double integral in equation (36) is performed to consider all possible pairs of direct/diffracted beams. In the perfectly coherent case, T_{cc} becomes

$T_{cc}(\mathbf{Q}, \mathbf{Q}') = t(\mathbf{Q})\, t^*(\mathbf{Q}') = A(\mathbf{Q})\, A(\mathbf{Q}') \exp[-i\chi(\mathbf{Q}) + i\chi(\mathbf{Q}')]$, and thus equation (36) is identical to equation (33). T_{cc} accompanied by the partial coherent effect can be obtained by integrating T_{cc} in a perfectly coherent case over both the spread of the illumination direction causing spatial incoherence and the defocus spread causing temporal incoherence (Ishizuka, 1980; Kirkland, 2020),

$$T_{cc}(\mathbf{Q}, \mathbf{Q}') = A(\mathbf{Q})\, A(\mathbf{Q}') \exp[-i\chi(\mathbf{Q}) + i\chi(\mathbf{Q}')]$$
$$\times E_S(\mathbf{Q}, \mathbf{Q}')\, E_C(\mathbf{Q}, \mathbf{Q}'), \qquad (37)$$

where $E_S(\mathbf{Q}, \mathbf{Q}')$ and $E_C(\mathbf{Q}, Q')$ are the envelope functions given as

$$E_S(\mathbf{Q}, \mathbf{Q}') =$$
$$\exp\left\{-\pi^2\beta^2\left[\Delta f(\mathbf{Q}-\mathbf{Q}') + \lambda^2 C_s\left(|\mathbf{Q}|^2\mathbf{Q} - |\mathbf{Q}'|^2\mathbf{Q}'\right)\right]^2\right\}, \quad (38)$$

$$E_C(\mathbf{Q}, \mathbf{Q}') = \exp\left\{-\left[\pi\lambda C_c(\Delta E/E)\right]^2\left(|\mathbf{Q}|^2 - |\mathbf{Q}'|^2\right)^2/2\right\}. \quad (39)$$

C_c is the chromatic aberration coefficient and ΔE is the $1/e$ width of the energy spread of incident electrons assuming a Gaussian distribution, and they are related to the defocus spread. β is the illumination semi-angle due to the finite source size effect. Although we should additionally include the contribution of the instability of the lens current in the defocus spread term, this contribution is neglected in *ReciPro*.

E2. Linear image model

The linear image model is a further simplified expression of the TCC model, in which the partial coherence terms $E_S(\mathbf{Q}, \mathbf{Q}')$ and $E_C(\mathbf{Q}, \mathbf{Q}')$ are replaced by $E_S(\mathbf{Q}, 0)\, E_S(\mathbf{Q}', 0)$ and $E_C(\mathbf{Q}, 0)\, E_C(\mathbf{Q}', 0)$, respectively. Within this approximation, $T_{cc}(\mathbf{Q}, \mathbf{Q}')$ can be rewritten as

$$T_{cc}(\mathbf{Q}, \mathbf{Q}') = T(\mathbf{Q})\, T^*(\mathbf{Q}'), \qquad (40)$$

where $T(\mathbf{Q}) = A(\mathbf{Q})\exp[-i\chi(\mathbf{Q})]\, E_S(\mathbf{Q}, 0)\, E_C(\mathbf{Q}, 0)$. Thus, the HRTEM image intensity is described as

$$I(\mathbf{R}) = \left|\mathcal{F}_{\mathbf{Q}\to\mathbf{R}}^{-1}[\psi(\mathbf{Q}, t)\, T(\mathbf{Q})]\right|^2. \qquad (41)$$

The benefit of this model is that the partial coherence effect is simply included in the point spread function, and the HRTEM image intensity can be calculated from the squared amplitude of the inverse Fourier transform of the convolution product between the exit wavefunction and the point spread function, instead of the cumbersome double integral in equation (36).

The linear image model does not correctly introduce the effect of partial coherence on the interference between nonzero $\mathbf{Q}$ and $\mathbf{Q}'$ components (*i.e.* a pair of diffracted beams), although the effect is accurately calculated when either $\mathbf{Q}$ or $\mathbf{Q}'$ is zero (*i.e.* either of them is the direct beam). Therefore, the linear image model is preferable for application to image simulations for a thin sample in which the weak phase object approximation holds, whereas the TCC model should be used for a strong scattering object which usually excites many strong diffracted beams.

References

Allen, L. J., Findlay, S. D., Oxley, M. P. & Rossouw, C. J. (2003). *Ultramicroscopy*, **96**, 47–63.

Allen, L. J. & Rossouw, C. J. (1989). *Phys. Rev. B*, **39**, 8313–8321.

Aroyo, M. I. (2016). Editor. *International Tables for Crystallography*, Vol. A, *Space-Group Symmetry*, 6th ed. Chichester: Wiley.

Barthel, J. (2018). *Ultramicroscopy*, **193**, 1–11.

Bethe, H. (1928). *Ann. Phys.* **392**, 55–129.

Bird, D. M. & King, Q. A. (1990). *Acta Cryst.* A**46**, 202–208.

Brown, H., Pelz, P., Ophus, C. & Ciston, J. (2020). *Microsc. Microanal.* **26**, 2954–2956.

Buxton, B. F., Eades, J. A., Steeds, J. W. & Rackham, G. M. (1976). *Philos. Trans. R. Soc. London Ser. A*, **281**, 171–194.

Carter, C. B. & Williams, D. B. (2016). *Transmission Electron Microscopy: Diffraction, Imaging, and Spectrometry*. Cham: Springer International Publishing.

Chantler, C. T. (1995). *J. Phys. Chem. Ref. Data*, **24**, 71–643.

Downs, R. T. & Hall-Wallace, M. (2003). *Am. Mineral.* **88**, 247–250.

Fujimoto, F. (1959). *J. Phys. Soc. Jpn*, **14**, 1558–1568.

Fultz, B. & Howe, J. M. (2013). *Transmission Electron Microscopy and Diffractometry of Materials*, 4th ed. Berlin, Heidelberg: Springer Verlag.

Hall, C. R. & Hirsch, P. B. (1965). *Proc. R. Soc. London Ser. A*, **286**, 158–177.

Hall, S. R. (1984). *Acta Cryst.* A**40**, C455.

Higham, N. J. (2005). *SIAM J. Matrix Anal. Appl.* **26**, 1179–1193.

Humphrey, W., Dalke, A. & Schulten, K. (1996). *J. Mol. Graph.* **14**, 33–38.

Hÿtch, M. J. & Stobbs, W. M. (1994). *Ultramicroscopy*, **53**, 191–203.

Ishizuka, K. (1980). *Ultramicroscopy*, **5**, 55–65.

Ishizuka, K. (2002). *Ultramicroscopy*, **90**, 71–83.

Ishizuka, K. & Uyeda, N. (1977). *Acta Cryst.* A**33**, 740–749.

Juhás, P., Farrow, C., Yang, X., Knox, K. & Billinge, S. (2015). *Acta Cryst.* A**71**, 562–568.

Kilaas, R., O'Keefe, M. A. & Krishnan, K. M. (1987). *Ultramicroscopy*, **21**, 47–61.

Kim, H. S. & Sheinin, S. S. (1982). *Phys. Status Solidi B*, **109**, 807–816.

Kirkland, E. J. (2020). *Advanced Computing in Electron Microscopy*, 3rd ed. Cham: Springer Nature Switzerland AG.

Koch, C. T. (2002). PhD thesis, Arizona State University, USA.

Kokalj, A. (1999). *J. Mol. Graph.* **17**, 176–179.

Kuramochi, K. (2009). PhD thesis, Tokyo University of Science, Japan.

Larsen, A. H., Mortensen, J. J., Blomqvist, J., Castelli, I. E., Christensen, R., Dułak, M., Friis, J., Groves, M. N., Hammer, B., Hargus, C., Hermes, E. D., Jennings, P. C., Bjerre Jensen, P., Kermode, J., Kitchin, J. R., Leonhard Kolsbjerg, E., Kubal, J., Kaasbjerg, K., Lysgaard, S., Bergmann Maronsson, J., Maxson, T., Olsen, T., Pastewka, L., Peterson, A., Rostgaard, C., Schiøtz, J., Schütt, O., Strange, M., Thygesen, K. S., Vegge, T., Vilhelmsen, L., Walter, M., Zeng, Z. H. & Jacobsen, K. W. (2017). *J. Phys. Condens. Matter*, **29**, 273002.

Lobato, I. & Van Dyck, D. (2015). *Ultramicroscopy*, **156**, 9–17.

Madsen, J. & Susi, T. (2021). *Open Res. Eur.* **1**, 24.

Midgley, P. A. & Eggeman, A. S. (2015). *IUCrJ*, **2**, 126–136.

Momma, K. & Izumi, F. (2011). *J. Appl. Cryst.* **44**, 1272–1276.

Ohtsuka, M. (2013). PhD thesis, Tokyo University of Science, Japan.

Ohtsuka, M., Yamazaki, T., Kotaka, Y., Fujisawa, H., Shimizu, M., Honda, K., Hashimoto, I. & Watanabe, K. (2013). *Acta Cryst.* A**69**, 289–296.

Ong, S. P., Richards, W. D., Jain, A., Hautier, G., Kocher, M., Cholia, S., Gunter, D., Chevrier, V. L., Persson, K. A. & Ceder, G. (2013). *Comput. Mater. Sci.* **68**, 314–319.

Oxley, M. P., Cosgriff, E. C. & Allen, L. J. (2005). *Phys. Rev. Lett.* **94**, 203906.

Peng, L.-M. (1998). *Acta Cryst.* A**54**, 481–485.

Peng, L.-M., Ren, G., Dudarev, S. L. & Whelan, M. J. (1996). *Acta Cryst.* A**52**, 257–276.

Pennington, R. S., Wang, F. & Koch, C. T. (2014). *Ultramicroscopy*, **141**, 32–37.

Pennycook, S. J. & Jesson, D. E. (1991). *Ultramicroscopy*, **37**, 14–38.

Prince, E. (2004). Editor. *International Tables for Crystallography*, Vol. C, *Mathematical, Physical and Chemical Tables*, 3rd ed. Dordrecht: Kluwer Academic Publishers.

Pryor, A., Ophus, C. & Miao, J. W. (2017). *Adv. Struct. Chem. Imag.* **3**, 15.

Rietveld, H. M. (1969). *J. Appl. Cryst.* **2**, 65–71.

Stadelmann, P. A. (1987). *Ultramicroscopy*, **21**, 131–145.

Sturkey, L. (1962). *Proc. Phys. Soc.* **80**, 321–354.

Thust, A. (2009). *Phys. Rev. Lett.* **102**, 220801.

Vincent, R. & Midgley, P. A. (1994). *Ultramicroscopy*, **53**, 271–282.

Waasmaier, D. & Kirfel, A. (1995). *Acta Cryst.* A**51**, 416–431.

Watanabe, K., Yamazaki, T., Hashimoto, I. & Shiojiri, M. (2001). *Phys. Rev. B*, **64**, 115432.

Weickenmeier, A. & Kohl, H. (1991). *Acta Cryst.* A**47**, 590–597.

Williams, D. B. & Carter, C. B. (2009). *Transmission Electron Microscopy: a Textbook for Materials Science*, 2nd ed. New York: Springer Science + Business Media.

Yamazaki, T., Ohtsuka, M., Kotaka, Y. & Watanabe, K. (2013). *Ultramicroscopy*, **135**, 16–23.

Yoshioka, H. (1957). *J. Phys. Soc. Jpn*, **12**, 618–628.

Zuo, J. M. & Spence, J. C. H. (2017). *Advanced Transmission Electron Microscopy: Imaging and Diffraction in Nanoscience*. New York: Springer Science + Business Media.